

# Laser-induced terahertz spin transport in magnetic nanostructures arises from the same force as ultrafast demagnetization

S.M. Rouzegar<sup>1,2</sup>, L. Brandt<sup>3</sup>, L. Nádvorník<sup>1,2,4</sup>, D.A. Reiss<sup>1</sup>, A.L. Chekhov<sup>1,2</sup>, O. Gueckstock<sup>1,2</sup>, C. In<sup>1,2</sup>, M. Wolf<sup>2</sup>, T.S. Seifert<sup>1</sup>, P.W. Brouwer<sup>1</sup>, G. Woltersdorf<sup>3</sup>, T. Kampfrath<sup>1,2</sup>

1. Department of Physics, Freie Universität Berlin, 14195 Berlin, Germany
2. Department of Physical Chemistry, Fritz Haber Institute of the Max Planck Society, 14195 Berlin, Germany
3. Institut für Physik, Martin-Luther-Universität Halle, 06120 Halle, Germany
4. Faculty of Mathematics and Physics, Charles University, Ke Karlovu 3, 121 16 Prague, Czech Republic

## Abstract

Laser-induced terahertz spin transport (TST) and ultrafast demagnetization (UDM) are central but so far disconnected phenomena in femtomagnetism and terahertz spintronics. Here, we show that UDM and TST are driven by the same force: a generalized spin voltage, which is induced by the incident femtosecond laser pulse. Using broadband terahertz emission spectroscopy, we find that the rate of UDM of a single ferromagnetic film F has the same time evolution as the flux of TST from F into an adjacent normal-metal layer N. An analytical model consistently and quantitatively explains our observations. It reveals that both UDM in F and TST in the F|N stack arise from a generalized spin voltage  $\Delta\tilde{u}_s$ , which is defined for arbitrary, nonthermal electron distributions. Our findings open up unexpected synergies and new pathways toward large-amplitude terahertz spin currents and, thus, energy-efficient ultrafast spintronic devices.

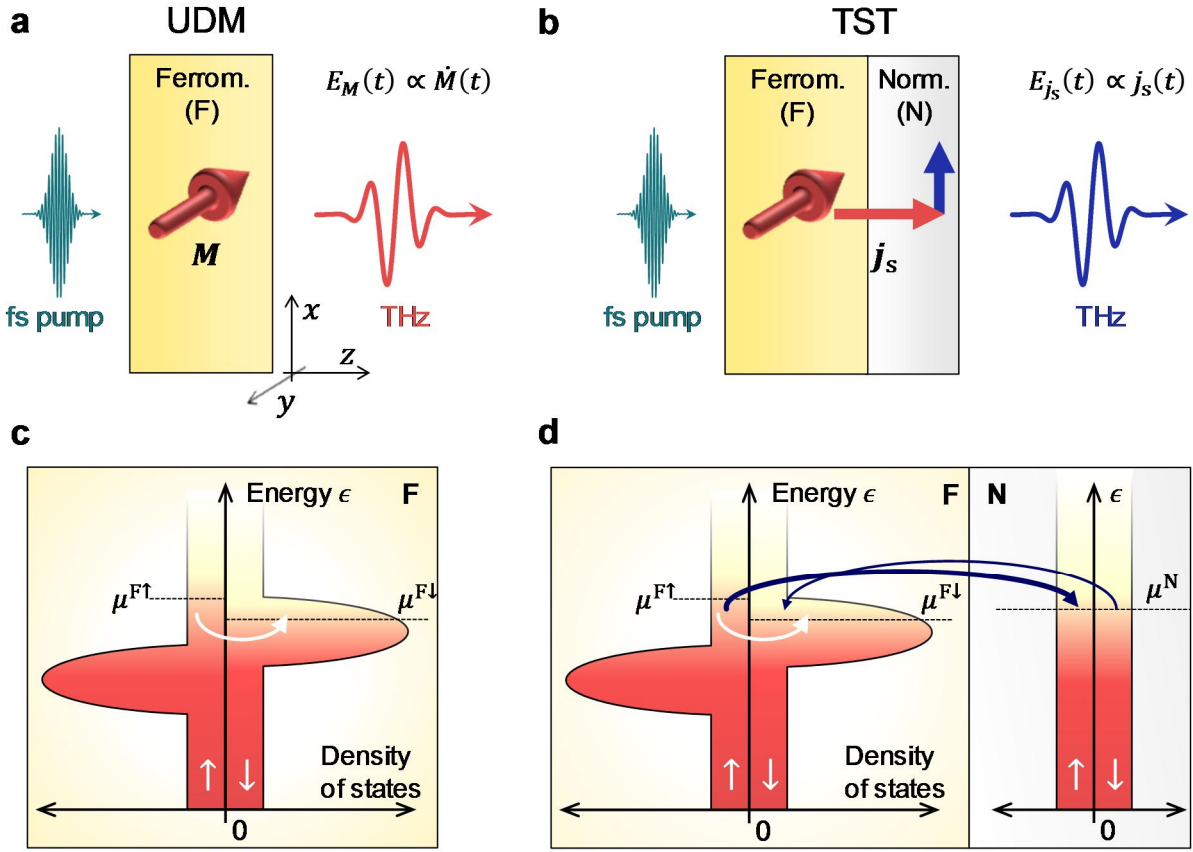


**Figure 1 | Ultrafast demagnetization (UDM) vs terahertz spin transport (TST).** **(a)** Side view of a single ferromagnetic metal layer (F) with magnetization  $\mathbf{M} = M\mathbf{u}_y$  parallel to the  $y$  axis with unit vector  $\mathbf{u}_y$ . Excitation by a femtosecond laser pulse triggers UDM. The transient magnetic dipole gives rise to the emission of a terahertz pulse with field  $E_M(t) \propto \dot{M}(t)$ . **(b)** F|N stack consisting of F and an adjacent normal paramagnetic metal layer (N). Femtosecond laser excitation drives a spin current with density  $j_s = j_s \mathbf{u}_z$  from F to N. In N,  $j_s$  is converted into a charge current with density  $j_c$ , leading to the emission of a terahertz electromagnetic pulse with electric field  $E_{j_s}(t) \propto j_s(t)$  directly behind the sample. Both  $E_M(t)$  and  $E_{j_s}(t)$  are linearly polarized perpendicular to  $\mathbf{M}$  and measured by electrooptic sampling. **(c)** Schematic of the density of states of spin-up and spin-down electrons of a Stoner-type ferromagnet such as Fe. Quasi-elastic spin-flip scattering events (white curved arrow) lead to transfer of spin angular momentum to the crystal lattice. **(d)** N acts as an additional sink of spin angular momentum through spin-conserving electron transfer across the F|N interface (blue curved arrows). In (a) and (b), the spin transfer rate scales with the generalized spin voltage  $\Delta\tilde{\mu}_s$  (Eq. (4)), which equals  $\mu^{F\uparrow} - \mu^{F\downarrow}$  in the case of Fermi-Dirac electron distributions.

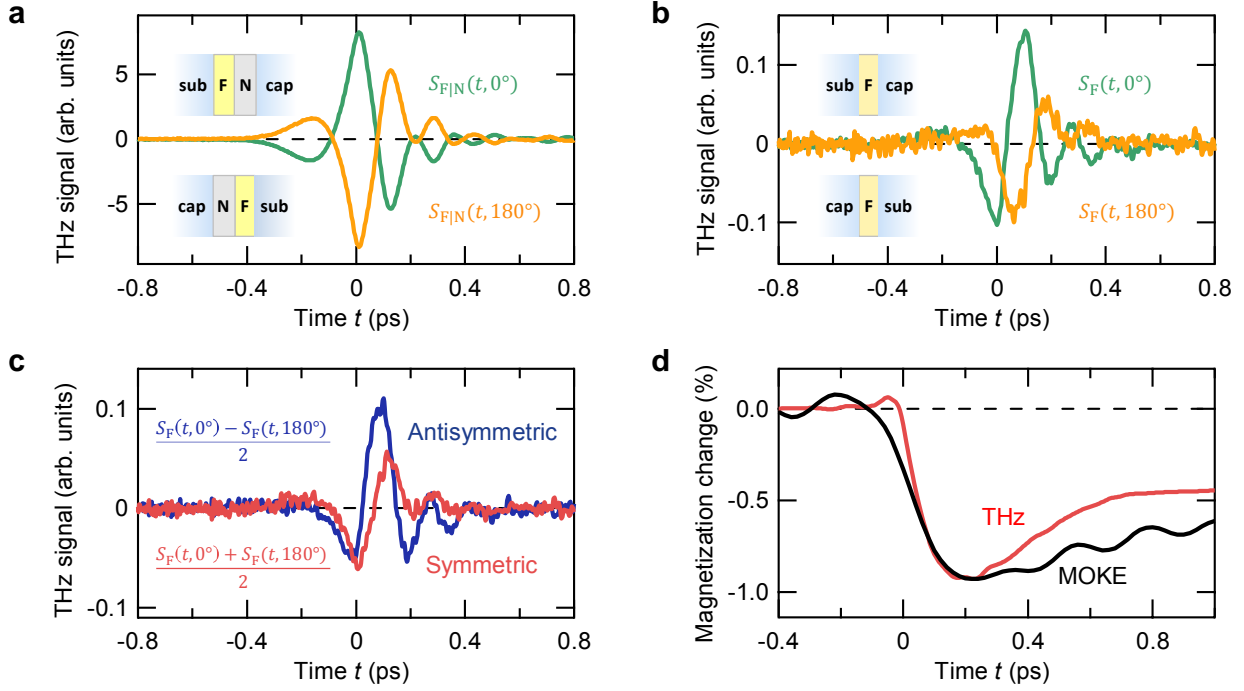


**Figure 2 | Terahertz emission from F and F|N films.** Typical terahertz electrooptic signals, odd with respect to magnetization  $M$ , from samples consisting of F=CoFe(3 nm) and N=Pt(3 nm). **(a)** Terahertz emission signal  $S_{F|N}(t, 0^\circ)$  from an F|N stack. When the sample is turned by  $180^\circ$  about  $M$ , the signal  $S_{F|N}(t, 180^\circ)$  is obtained. Note that the sample is optically symmetrized by a cap window that is identical to the diamond substrate. **(b)** Same as panel (a), but for the F sample. Note the asymmetry between  $S_F(t, 0^\circ)$  and  $S_F(t, 180^\circ)$ . **(c)** Signals  $S_F^+(t)$  and  $S_F^-(t)$  symmetric and antisymmetric with respect to sample turning. **(d)** Extracted magnetization dynamics from the symmetric signal of panel (c) (red curve), along with magnetization dynamics as measured by the magnetooptic Kerr effect (MOKE, black curve).

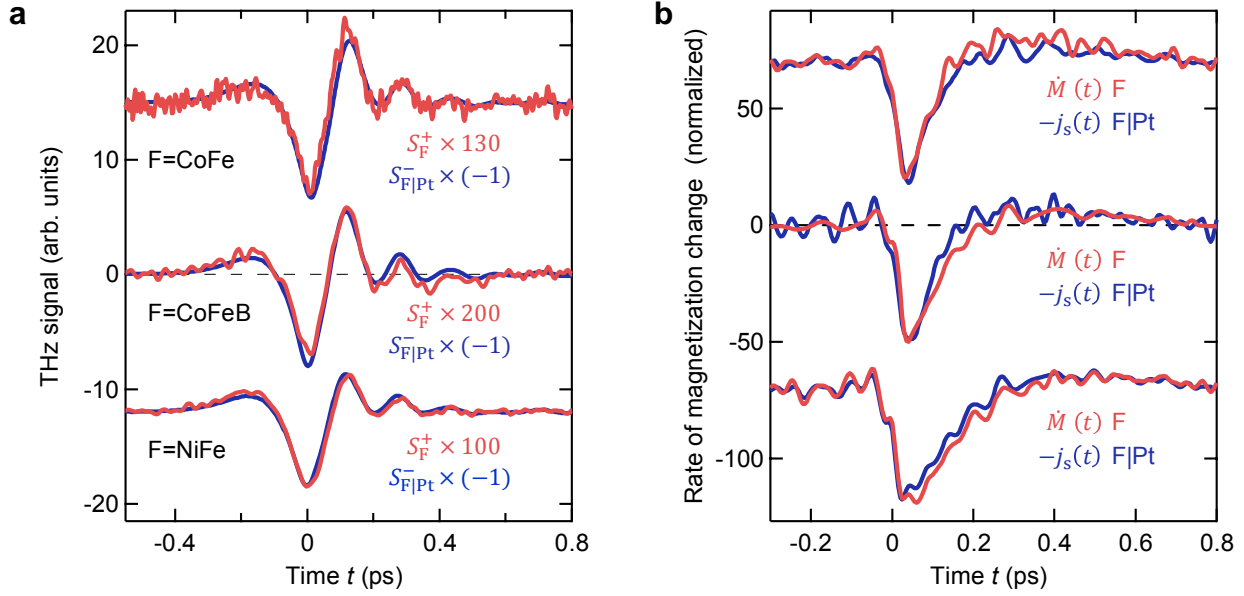


**Figure 3 | Terahertz emission due to TST in F|N vs UDM in F.** **(a)** Terahertz signal  $S_{F|N}^-(t)$  from a CoFe(3 nm)|Pt(3 nm) sample, antisymmetric with respect to sample turning about  $\mathbf{M}$  (red solid line), vs terahertz signal  $S_F^+(t)$  from a single CoFe(3 nm) layer, symmetric with respect to sample turning (blue solid line). The curves below show analogous signals for CoFeB(5 nm)|Pt(3 nm), CoFeB(5 nm) and NiFe(9 nm)|Pt(3 nm), NiFe(9 nm) samples. The curves are scaled by the indicated factors and offset vertically for clarity. **(b)** Temporal evolution of the spin current  $j_s$  flowing in the F|N sample and of the rate of change  $\dot{M}$  of the F sample's magnetization as extracted from the data of panel (a). Curves are normalized to their minima.

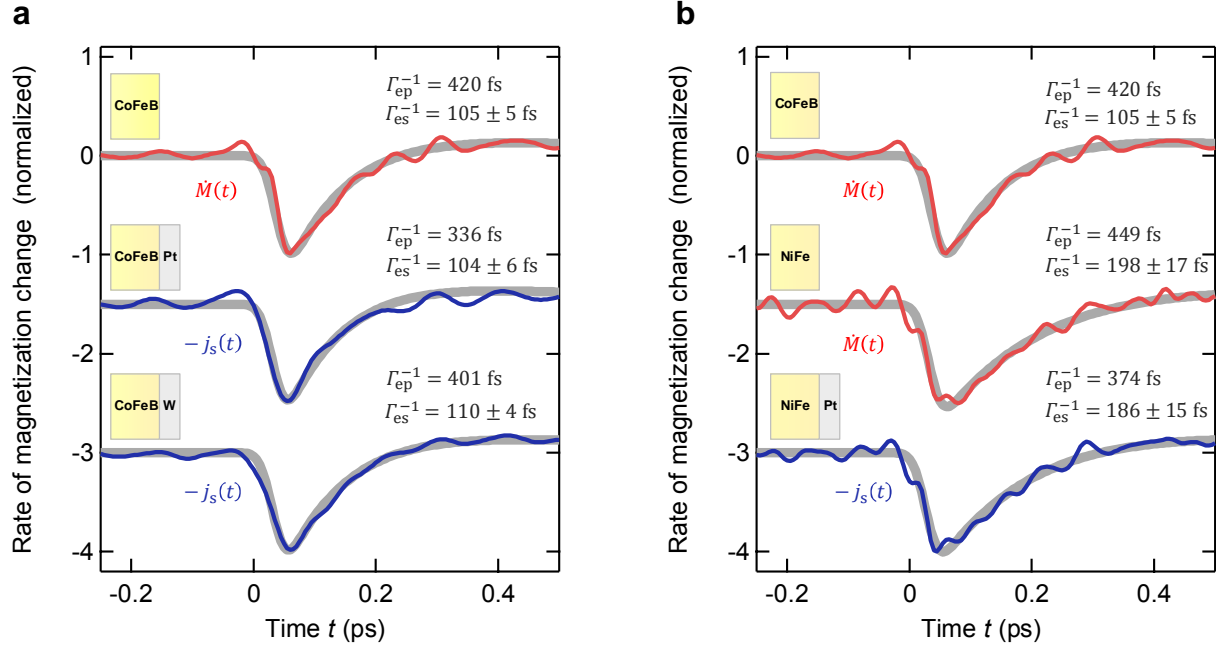


**Figure 4 | Measured and modeled dynamics of  $\dot{M}$  and  $j_s$ .** **(a)** Measured dynamics of the rate of change  $\dot{M}(t)$  of the magnetization of a CoFeB film (red solid line) and the spin current  $j_s(t)$  of CoFeB|Pt and CoFeB|W stacks (blue solid lines). Grey solid lines are fits based on Eq. (7) with  $\Gamma_{\text{es}}$  and the overall amplitude scaling as the only fit parameters. **(b)** Analogous to (a), but for CoFeB, NiFe and NiFe|Pt.

Fundamental operations in future spin-based electronics are the manipulation of magnetic order, the transport of spin angular momentum and the detection of spin dynamics.<sup>1</sup> The research fields of femtomagnetism and terahertz spintronics aim to push the three operations to femtosecond time scales and, thus, terahertz bandwidth.<sup>2,3,4,5,6</sup> Figures 1a,b show the model systems in which two key phenomena of ultrafast spin dynamics were studied extensively.

In a single ferromagnetic metal layer F, uniform excitation by a femtosecond laser pulse induces ultrafast demagnetization (UDM; Fig. 1a).<sup>2,7,8,9</sup> This effect reveals the time scales of elementary spin interactions with electron orbital and lattice degrees of freedom and is a central ingredient for ultrafast magnetization switching.<sup>3</sup> Theories of UDM involve spin flips<sup>7,10,11,12</sup> or magnon emission<sup>13</sup> due to electron scattering together with spin-orbit coupling.<sup>14</sup>

In F|N stacks, where N is a normal paramagnetic metal layer, uniform laser excitation triggers terahertz spin transport (TST) between F and N (Fig. 1b).<sup>4,6,15,16,17,18,19,20</sup> Such spin currents can exert spin torque at ultrashort time and length scales. They may, thus, excite terahertz magnons<sup>21,22</sup> and, ultimately, switch magnetic order.<sup>3</sup> TST also serves to efficiently generate broadband terahertz electromagnetic pulses for photonic and spectroscopy applications.<sup>23,24,25,26</sup> Simulations indicate that TST is an example of superdiffusive transport.<sup>27,28,29</sup>

Here, we use terahertz emission spectroscopy to reveal correlations between UDM in F samples (Fig. 1a) and TST in F|N stacks (Fig. 1b). Our experimental results along with an analytical model show that the seemingly disconnected fundamental phenomena of UDM and TST are driven by the same force: a generalized spin voltage of the electrons in F. These insights open up completely new perspectives and synergies because they allow us to better understand and ultimately optimize TST by exploiting the extensive knowledge about UDM.

### Experiment design

As F materials, we chose the Stoner-type ferromagnets  $\text{Co}_{70}\text{Fe}_{30}$  (CoFe),  $\text{Co}_{40}\text{Fe}_{40}\text{B}_{20}$  (CoFeB) and  $\text{Ni}_{80}\text{Fe}_{20}$  (NiFe). For N, we chose the spin-to-charge conversion materials Pt and W because they exhibit large yet opposite spin Hall angles.<sup>23</sup> Two thin films of F and F|N were grown on one diamond substrate, which is transparent at all relevant terahertz and optical frequencies.

Terahertz emission spectroscopy is an excellent approach to measure the dynamics of the magnetization  $\mathbf{M}(t) = M(t)\mathbf{u}_y$  of an F sample (Fig. 1a) and of the spin current flowing from F into an adjacent N (Fig. 1b) with very fine (40 fs) resolution of time  $t$ . UDM (Fig. 1a) implies a dynamic magnetic dipole that generates an electromagnetic pulse<sup>30,31</sup> with an electric field

$$E_M(t) \propto \dot{M}(t) \quad (1)$$

directly behind the sample (see Methods). For comparison, we also probed  $M(t)$  of the F sample by the transient magnetooptic Kerr effect (MOKE).

In TST (Fig. 1b), the spin-current density  $\mathbf{j}_s(t) = j_s(t)\mathbf{u}_z$  across the F-N interface is instantaneously converted<sup>32</sup> into a transverse charge-current density proportional to  $j_s(t)$  by the inverse spin Hall effect in N. It results in a time-dependent electric dipole and, thus, emission of an electromagnetic pulse with transient electric field<sup>23,24,25,26</sup>

$$E_{j_s}(t) \propto j_s(t). \quad (2)$$

As the dynamics are driven by a femtosecond laser pulse, the bandwidth of  $E_M$  and  $E_{j_s}$  is expected to extend to frequencies well above 10 THz. We detected the transient electric field  $E(t)$  by electrooptic sampling.<sup>33</sup> The resulting signal waveform  $S(t, \mathbf{M})$  is connected to  $E(t)$  by a linear response function that captures the propagation and detection of the terahertz field in our setup. To focus on magnetic effects, we only considered the signal component  $S(t) = [S(t, \mathbf{M}) - S(t, -\mathbf{M})]/2$ . By a calibration and inversion

procedure,<sup>34,35</sup> we determined the magnitude and direction of  $E(t)$  behind the sample and, eventually,  $\dot{M}(t)$  and  $j_s(t)$  with a time resolution of 40 fs (see Methods).

The total THz field behind the F|Pt and F|W stacks is dominated<sup>23</sup> by  $E_{j_s}$ . Due to its electric-dipole character,  $E_{j_s}(t)$  fully reverses when the F|N stack is turned by 180° about an axis parallel to  $\mathbf{M}$  (Fig. 1b). In contrast, the field  $E_M$  from the F sample originates from magnetic dipoles. It, thus, remains invariant under 180° sample turning (Fig. 1a) and is much smaller<sup>31</sup> than  $E_{j_s}$ . To minimize competing signals due to pump-induced gradients,<sup>36</sup> the F thickness was chosen sufficiently small. To discriminate electric-dipole signals due to a possible inversion asymmetry of the F sample,<sup>37</sup> we measured it both in the 0° and the 180°-turned configuration. For this purpose, the samples were macroscopically symmetrized by adding a cap layer (cap) that is identical to the substrate (sub; see inset of Fig. 2a and Methods).

### Terahertz emission signals

Figure 2a shows the signal  $S(t)$  from a sub||F|N||cap sample where F=CoFe(3 nm) and N=Pt(3 nm). As expected from Fig. 1b, the signal is antisymmetric with respect to turning the sample and, thus, reverses completely in the 180°-configuration cap||F|N||sub. We note that we actually used this antisymmetric behavior to precisely turn the sample around. Very similar signals were observed for W as N material (Fig. 4).

The terahertz signals from the F sample (Fig. 2b) are two orders of magnitude smaller than from the F|N counterpart. When the sample was turned, the signal did not simply invert but changed shape. This behavior indicates a superposition of contributions which are symmetric (+) and asymmetric (−) under sample turning. To separate them, we calculate the signals  $S_F^\pm(t) = [S_F(t, \theta = 0^\circ) \pm S_F(t, \theta = 180^\circ)]/2$  (Fig. 2c). We emphasize that we could reliably reproduce  $S_F^+(t)$  using two more complementary approaches (see Methods and Supplementary Note 1).

The magnitude of the asymmetric component  $S_F^-$  is comparable to that of  $S_F^+$  and suggests that the F sample exhibits noticeable inversion asymmetry. This conclusion is not unexpected because thin films are known to exhibit inhomogeneities along the growth direction and to possess different properties at the substrate interface as compared to the bulk.<sup>38</sup>

The symmetric component  $S_F^+(t)$  contains the contribution  $E_M$  due to UDM (Fig. 1a). Assuming that  $S_F^+$  solely arises from  $E_M$ , we retrieve  $E_M(t)$  and, thus, the evolution of the magnetization change  $\Delta M(t)$  (see Methods). The extracted  $\Delta M(t)$  is shown in Fig. 2d along with the magnetization dynamics measured by the transient MOKE (black curve in Fig. 2d). The good agreement of the two curves in terms of sign, magnitude and shape is fully consistent with the notion that  $S_F^+$  arises from UDM of the F sample.

We can now directly compare the terahertz signal waveforms  $S_F^+(t)$  and  $S_{F|N}^-(t)$  due to UDM of a single layer of F=CoFe (Fig. 1a) and TST from F into N (Fig. 1b). The result is shown in Fig. 3a and reveals a remarkable correlation: The terahertz signals  $S_F^+(t)$  and  $S_{F|N}^-(t)$  exhibit completely identical dynamics. We emphasize that we made analogous observations for two other ferromagnets, F=CoFeB and NiFe (Fig. 3a), as well as N=W (Fig. 4b) and different film thicknesses.

Our observation  $S_{F|N}^-(t) \propto S_F^+(t)$  and the origins of  $S_{F|N}^-$  (Eq. (1)) and  $S_F^+$  (Eq. (2)) imply that

$$j_s(t) \propto \dot{M}(t). \quad (3)$$

In other words, our THz emission signals show directly that on ultrafast time scales, the photoinduced spin current in an F|N stack has a temporal evolution that is identical to that of the rate of photoinduced magnetization quenching of an F sample. The most explicit manifestation of Eq. (3) is Fig. 3b, which shows the actual dynamics of  $j_s$  and  $\dot{M}$  as retrieved from the signals  $S_{F|N}^-$  and  $S_F^+$ .

Equation (3) summarizes our central experimental result and reveals the profound relationship between UDM (Fig. 1a) and TST (Fig. 1b). It strongly suggests that TST in an F|N stack and UDM of an F sample are driven by the same force.

### Driving force

To identify this force, we temporarily assume that the photoexcited electrons in the F and F|N sample can be described by an instantaneous electron temperature  $T_e$  that is equal for spin-up ( $\uparrow$ ) and spin-down ( $\downarrow$ ) electrons in F and N. Recent works<sup>11,19,39</sup> found that a pump-induced increase of  $T_e$  leads to a shift of the chemical potentials  $\mu^{F\uparrow}$  and  $\mu^{F\downarrow}$  of majority- and minority-spin electrons in the F region, respectively (Fig. 1c). Because  $\uparrow$  and  $\downarrow$  electrons in a ferromagnet have a different band structure, a transient nonequilibrium state with  $\mu^{F\uparrow} \neq \mu^{F\downarrow}$  and, thus, a nonvanishing spin voltage<sup>39</sup>  $\mu^{F\uparrow} - \mu^{F\downarrow}$  results.

Mueller *et al.*<sup>40</sup> concluded and Choi *et al.*<sup>19</sup> assumed that in F, a positive  $\mu^{F\uparrow} - \mu^{F\downarrow}$  drives UDM since it enables more spin-flip scattering events of  $\uparrow$  electrons into  $\downarrow$  electronic states than vice versa<sup>11</sup> (Fig. 1c). At the interface of an F|N stack, on the other hand, a positive  $\mu^{F\uparrow} - \mu^{F\downarrow}$  is known to drive TST into N<sup>19,41</sup> because of a net difference of electron transmission events through the interface (Fig. 1d). The rate of the local UDM<sup>11</sup> (Fig. 1c) and the flux of TST<sup>19,41</sup> (Fig. 1d) are both directly proportional to the spin voltage, that is,  $\dot{M} \propto j_s \propto \mu^{F\uparrow} - \mu^{F\downarrow}$ . This conclusion is in striking agreement with our experimental results (Fig. 3 and Eq. (3)).

Importantly, the preceding consideration can be generalized to nonthermal electron distributions that cannot be described by Fermi-Dirac functions. We determine  $\dot{M}(t)$  and  $j_s(t)$  by counting the spin flips in F (Methods and Fig. 1c) and the electron transmission events through the F-N interface (Fig. 1d). Provided the scattering processes are quasi-elastic<sup>7</sup> and the pump pulse can be considered a small perturbation of the system, we find that

$$\dot{M}(t), j_s(t) \propto \Delta\tilde{\mu}_s(t) + (\text{Seebeck terms}). \quad (4)$$

Here, the quantity  $\Delta\tilde{\mu}_s$  is given by

$$\Delta\tilde{\mu}_s(t) = \int d\epsilon (n^{F\uparrow} - n^{F\downarrow})(\epsilon, t), \quad (5)$$

where  $n^{F\sigma}(\epsilon, t) = n_0(\epsilon) + \Delta n^{F\sigma}(\epsilon, t)$  denotes the occupation number of a Bloch state with spin  $\sigma$  ( $\uparrow$  or  $\downarrow$ ) and energy  $\epsilon$  in F. It is a sum of the distribution  $n_0$  of the unexcited sample and the pump-induced changes  $\Delta n^{F\sigma}$ . If the  $n^{F\sigma}$  are Fermi-Dirac-type functions with temperature  $T_e$  and chemical potentials  $\mu^{F\sigma}$ , Eq. (5) yields the conventional result  $\Delta\tilde{\mu}_s = \mu^{F\uparrow} - \mu^{F\downarrow}$  (see Methods). Therefore,  $\Delta\tilde{\mu}_s$  can be considered as a generalized spin voltage that is caused by an electron distribution with an arbitrary (nonthermal) pump-induced imbalance  $\Delta n^{F\uparrow} - \Delta n^{F\downarrow}$ .

In the case of  $\dot{M}(t)$ , the Seebeck-type term in Eq. (4) is proportional to the difference  $\Delta\tilde{T}^{F\uparrow} - \Delta\tilde{T}^{F\downarrow}$ , while for  $j_s(t)$ , it equals a linear combination of  $\Delta\tilde{T}^{F\uparrow} - \Delta\tilde{T}^{N\uparrow}$  and  $\Delta\tilde{T}^{F\downarrow} - \Delta\tilde{T}^{N\downarrow}$ . Here,  $\Delta\tilde{T}^{X\sigma}$  is the pump-induced change in the generalized temperature of electrons with spin  $\sigma$  in X=F or N. It scales with the electronic excess energy (Eq. (38)) and equals the conventional temperature change once the electron distribution is thermal.

Notably, while the spin voltage has the same form for  $\dot{M}(t)$  and  $j_s(t)$ , the Seebeck contribution is different. Therefore, our experimental results (Fig. 3 and Eq. (3)) strongly indicate that the Seebeck terms play a minor role in our experiment, possibly because all electronic subsystems  $X\sigma$  attain approximately equal generalized temperatures faster than our time resolution of 40 fs. Consequently, we consider only one common generalized electron temperature  $\Delta\tilde{T}^{X\sigma} = \Delta\tilde{T}_e$  in the following.

To conclude, our observations (summarized by Eq. (3)) and modeling (leading to Eq. (4)) imply that the generalized spin voltage  $\Delta\tilde{\mu}_s$  of F is the dominant driving force of both UDM (Fig. 1a) and TST (Fig. 1b).

## Modeling the dynamics

The identical temporal evolution of  $\Delta\tilde{\mu}_s$  in the F and F|N samples indicates that the coupling to the N layer does not significantly perturb the dynamics of (i) spins and (ii) electrons in F. For a quantitative discussion, we relate the generalized spin voltage  $\Delta\tilde{\mu}_s$  to the dynamics of the uniform generalized electron excess temperature  $\Delta\tilde{T}_e$  (see Methods). We obtain

$$\Delta\tilde{\mu}_s(t) \propto \Delta\tilde{T}_e(t) - \Gamma_{es} \int_0^\infty d\tau e^{-\Gamma_{es}\tau} \Delta\tilde{T}_e(t-\tau), \quad (6)$$

where  $\Gamma_{es}^{-1}$  is the time constant of electron-spin equilibration. To illustrate Eq. (6), we consider a step-like increase of the generalized uniform electron temperature. Once  $\Delta\tilde{T}_e$  jumps to a nonzero value,  $\Delta\tilde{\mu}_s(t)$  follows instantaneously according to the first term of Eq. (6), thereby triggering transfer of spin angular momentum from the F electrons into the F lattice (UDM) and, possibly, into N (TST). The loss of spin polarization, however, decreases  $\Delta\tilde{\mu}_s$ , which decays on the time scale  $\Gamma_{es}^{-1}$ , as dictated by the second term of Eq. (6).

It is known<sup>42,43</sup> that the excess energy of the F electrons and, thus, their generalized temperature  $\Delta\tilde{T}_e$  rise instantaneously upon pump-pulse excitation, and that they decay due to transfer to the crystal lattice. Thus, in remarkable contrast to the interfacial spin Seebeck effect,<sup>35</sup> carrier multiplication is irrelevant here (Eq. (6)). We accordingly model the evolution of  $\Delta\tilde{T}_e$  by  $\Delta\tilde{T}_e(t) \propto \Theta(t)[(1-R)e^{-\Gamma_{ep}t} + R]$  where  $\Theta(t)$  is the Heaviside step function,  $\Gamma_{ep}^{-1}$  is the time constant of electron-phonon equilibration, and  $R$  is the ratio of electronic and total heat capacity of the sample.

With these assumptions, Eqs. (4) and (6) yield the simple result

$$\dot{M}(t), j_s(t) \propto \Theta(t)[A_{es}e^{-\Gamma_{es}t} - A_{ep}e^{-\Gamma_{ep}t}], \quad (7)$$

where  $A_{es} = (\Gamma_{es} - R\Gamma_{ep})/(\Gamma_{es} - \Gamma_{ep})$  and  $A_{ep} = (1-R)\Gamma_{ep}/(\Gamma_{es} - \Gamma_{ep})$ . To account for our experimental time resolution, Eq. (7) is convoluted with a Gaussian of 40 fs full width at half maximum. We apply Eq. (7) to the measured  $\dot{M}(t)$  and  $j_s(t)$  (Fig. 4) and take only  $\Gamma_{es}$  and the overall amplitude as free sample-dependent fit parameters. For  $\Gamma_{ep}$  and  $R$ , literature values are assumed (see Methods and Table S2). Figure 4 demonstrates that Eq. (7) excellently describes the measured  $\dot{M}(t)$  and  $j_s(t)$ .

## Discussion

We can now discuss the impact of N on the dynamics of (i) the electron spins through  $\Gamma_{es}$  and (ii) the electronic excess heat through  $\Gamma_{ep}$ . According to Eq. (7), the slope of  $\dot{M}(t)$  and  $j_s(t)$  approximately equals  $-(\Gamma_{es} + \Gamma_{ep})$  right after excitation because both electron-spin and electron-phonon equilibration contribute to the decay dynamics. For an F sample with F=CoFeB, we find  $\Gamma_{es}^{-1} = 104$  fs (Fig. 4a), which agrees with previous reports<sup>44</sup> and is four times smaller than  $\Gamma_{ep}^{-1} = 420$  fs. Therefore,  $\Gamma_{es} \gg \Gamma_{ep}$ , and the slope of the initial decay of  $\dot{M}(t)$  is dominated by  $\Gamma_{es}$ .

When N=Pt is attached to CoFeB, we expect a larger  $\Gamma_{es}$  (due to TST) and an increase of  $\Gamma_{ep}$  by 20% (see Table S2). In contrast, we observe an equally fast decay of  $\dot{M}(t)$  and  $j_s(t)$  (Fig. 4a). Therefore, the time constant  $\Gamma_{es}^{-1}$  of the F|N sample does not decrease markedly as confirmed by our fits, which yield a very similar  $\Gamma_{es}^{-1}$  for CoFeB and CoFeB|Pt. In other words, TST into the Pt layer does not accelerate spin-electron equilibration ( $\Gamma_{es}$ ), and the slightly faster electron cooling ( $\Gamma_{ep}$ ) is negligible because  $\Gamma_{ep} \ll \Gamma_{es}$ . This reasoning is fully confirmed by the almost identical spin-current dynamics  $j_s(t)$  in CoFeB|W and CoFeB|Pt (Fig. 4a).

We finally test NiFe as F material because its  $\Gamma_{es}$  is smaller than for CoFeB.<sup>45</sup> Indeed, both  $\dot{M}(t)$  and  $j_s(t)$  decay 50% more slowly for NiFe than for CoFeB (Fig. 4b) while  $\Gamma_{es}$  remains the same for NiFe|Pt and NiFe within our experimental uncertainty.

## Conclusions

Our experiments show that, following optical excitation, the rate of change  $\dot{M}(t)$  of the magnetization of an F sample (Fig.1a) and the spin current density  $j_s(t)$  from F to an adjacent N (Fig.1b) exhibit identical dynamics. According to our analysis, this behavior relies on two reasons.

First, UDM and TST are driven by the same force: a generalized spin voltage (Eq. (4)). To quantitatively explain our data, we neither have to assume a temperature difference between F and N nor between majority and minority electrons in F. Therefore, our measured spin current is not the result of a spin-dependent Seebeck effect.<sup>41</sup> It is more adequate to term it an incoherent form of optically induced spin transfer (OISTR), as a slight generalization of the previously introduced term optical intersite spin transfer with the same acronym.<sup>46</sup>

Second, after the pump pulse has excited the electron system of F,  $\dot{M}(t)$  and  $j_s(t)$  jump to a nonzero value and subsequently relax by electron-spin equilibration, while the significantly slower electron-phonon equilibration has a minor impact. Our results strongly suggest that the impact of TST on  $\Gamma_{es}$  is minor in our experiments.

The last conclusion agrees with previous spin-transport works<sup>47</sup> and implies that in the F|N stack, the photoinduced spin voltage primarily decays due to spin-flip processes in F. In other words, only a small fraction of the available spin angular momentum is transferred into the N layer. There is, thus, large potential to considerably increase the spin-current amplitudes.

Importantly, our study allows us to apply the extensive knowledge about UDM of F samples to TST from F to an adjacent N layer. This insight is expected to be extremely helpful to boost spin-current amplitudes in numerous applications such as spin torque,<sup>3,4,21,22</sup> spintronic terahertz emitters<sup>23,24,25,26</sup> and, potentially, energy harvesting.<sup>48</sup> Our findings also provide a new straightforward link between concepts of femtomagnetism and spintronics. In particular, terahertz emission spectroscopy holds great promise to be an excellent ultrafast monitor of the evolution of the generalized spin voltage.

## Methods

**Sample preparation and characterization.** The F samples (where F is  $\text{Co}_{60}\text{Fe}_{20}\text{B}_{20}$ ,  $\text{Co}_{70}\text{Fe}_{30}$  or  $\text{Ni}_{80}\text{Fe}_{20}$ ) and F|N stacks (where N is Pt or W) were grown by means of magnetron sputtering. The deposition was performed with an Ar pressure of  $4 \times 10^{-3}$  mbar at growth rates between 0.2 Å/s and 1 Å/s, depending on the material. Half of the substrate was covered by a metallic mask during deposition of the N material, thereby resulting in an F sample and an F|N stack on the same substrate and in the same run. All samples were protected by a 10 nm thick  $\text{Al}_2\text{O}_3$  layer grown by atomic layer deposition. As substrates, we chose diamond and, for test purposes, fused silica.

Hysteresis loops showed that the samples have a coercive field below 10 mT. We also measured the optical absorptance  $A$  of the pump pulse and the sample impedance  $Z$  from 1 to 7 THz as detailed in Ref. 49. We found that  $Z$  was approximately independent of frequency. Values of  $A$ ,  $Z$  and the mean terahertz conductivity are compiled in Supplementary Table S3.

**Terahertz-emission setup.** The samples were excited with linearly polarized laser pulses (wavelength of 800 nm, duration of 10 fs and pulse energy of 2 nJ) from a Ti:sapphire laser oscillator (repetition rate at 80 MHz) under normal incidence. The pump beam diameter at the sample position was approximately 25  $\mu\text{m}$  full width at half maximum of the intensity.

The terahertz pulse emitted from the sample was detected by electrooptic sampling where a probe pulse (0.6 nJ, 10 fs) was copropagating with the terahertz pulse through an electrooptic crystal. The ellipticity  $S(t)$  accumulated by the sampling pulse was measured as a function of the delay  $t$  between terahertz and sampling pulse by means of a polarization-sensitive optical bridge consisting of a quarter-wave plate, a polarizing beam splitter and two balanced photodiodes. As electrooptic crystal, we used GaP(110) (thickness of 250  $\mu\text{m}$ ) if not explicitly mentioned otherwise, but also ZnTe(110) (thickness of 1 mm). All experiments were performed at room temperature in a dry  $\text{N}_2$  atmosphere.

**Measurement configurations.** The terahertz emission signal from the F|Pt and F|W samples is dominated by the electric-dipole field  $E_{j_s}$  (Fig. 1b). In contrast, the terahertz magnetic-dipole field  $E_M$  from the F sample (Fig. 1a) is typically two orders of magnitude smaller. It can easily be masked by spurious electric-dipole-type signals that arise when inversion symmetry is broken, either by the sample structure (structural inversion asymmetry, SIA) or by the perturbing light field (light-induced inversion asymmetry, LIA). For example, SIA can be caused by inequivalent interfaces of F,<sup>37</sup> and LIA can arise from a change of the pump intensity across the F thickness.<sup>36</sup>

To discriminate a terahertz electric-dipole field  $E_{\text{SIA}}$  due to SIA from  $E_M$ , three different approaches were implemented. In the first approach, we symmetrized the sample by adding a cap layer (cap) that is identical to the substrate (sub; see inset of Fig. 2a and Fig. S1a). We measured the sample both in the 0°-configuration sub||F||cap and the 180°-turned configuration cap||F||sub. While  $E_{\text{SIA}}$  changes sign,<sup>49</sup>  $E_M$  stays invariant. To minimize the field  $E_{\text{LIA}}$  owing to LIA, which is also invariant under sample turning, we chose an F thickness much thinner than the attenuation length of the optical pump field ( $\sim 30$  nm). Calculations show that in our metal stacks, the pump field changes by less than 5% over the full thickness of up to 10 nm.

We acquired terahertz emission data from the F sample and the associated F|N stack, both of which were grown on the same substrate and could be reached by translating the sample perpendicularly to the pump beam. As sample spots, we chose F and F|N regions as close as possible to guarantee identical optical environments for the probed F and F|N thin-film regions. To reproducibly put the metal film into the focal region of the pump spot, we used crossed beams of alignment lasers to mark the position and tilt angle of the sample. To test for correct alignment, we checked that the emission signals from the 0° and 180° sample configurations of the F|N sample were reversed versions of each other.

In the second approach, we measured unsymmetrized samples sub||F and sub||F|N analogous to the first method. Because of its macroscopic asymmetry, the signals from the 0° and 180° configurations of the

sub||F|N sample are in general not reversed versions of each other anymore. The two signals, are, however, connected by a transfer function that can be easily inferred and, in turn, applied to the two signals from the sub||F sample. More details and another separation method working in reflection mode are presented in Supplementary Note 1. We emphasize that all three separation methods delivered highly consistent results.

**From signals to fields to  $j_s$  and  $\dot{m}$ .** As detailed in Ref. 35, the measured electrooptic signal  $S(t)$  is connected to the terahertz electric field  $E(t)$  directly behind the sample by the convolution

$$S(t) = (H_{SE} * E)(t) = \int d\tau H_{SE}(t - \tau)E(\tau). \quad (8)$$

The transfer function  $H_{SE}(t)$  mediates between  $S$  and  $E$  and accounts for propagation to the detection and the electrooptic-sampling process.<sup>33</sup> We determined  $H_{SE}$  by using an appropriate reference emitter,<sup>34</sup> and by numerical inversion of Eq. (8),  $E$  was eventually obtained.

For the F|N stack, the signal is dominated by TST and the inverse spin Hall effect in the N layer, which converts the electron spin current with density  $(\hbar/2)j_s$  into a charge current with density  $(-e)j_c$ . Here,  $\hbar$  is the Planck constant,  $-e$  is the electron charge, and  $j_c = \theta_{SH}j_s$  with  $\theta_{SH}$  being the spin Hall angle of the N material. In the frequency domain, the terahertz electric field behind the sample is related to the spin current injected into the Pt layer by a generalized Ohm's law,<sup>23</sup>

$$E_{j_s}(\omega) = eZ(\omega)\theta_{SH}(\omega)\lambda_{rel}j_s(\omega). \quad (9)$$

Terahertz transmission measurements and broadband measurements of the anomalous Hall effect of magnetic metals<sup>32</sup> show that the sample impedance  $Z(\omega)$  and the spin Hall angle  $\theta_{SH}(\omega)$  are constant over the relevant frequency range. Therefore, Eq. (9) yields  $E_{j_s}(t) \propto j_s(t)$  in the time domain.

The time-dependent magnetization of the F sample gives rise to magnetic-dipole radiation with an electric field<sup>18</sup>

$$E_M(\omega) = -\frac{i\omega n d_F}{c} Z(\omega) M(\omega) \quad (10)$$

directly behind the sample. Here,  $n(\omega)$  is the refractive index of the half-space (substrate or cap window) that is not traversed by  $E_M$ ,  $d_F$  is the F thickness, and  $c$  is the speed of light. Because the refractive index of our substrate and cap windows and the impedance  $Z(\omega)$  are approximately independent of  $\omega$  for the terahertz frequencies relevant here, Eq. (10) leads to  $E_M(t) \propto \dot{M}(t)$  in the time domain.

**Optical probing of magnetization dynamics.** In this pump-probe measurement, pump and probe pulses were incident onto the sample under 50° angle of incidence. Pump pulses (duration of 200 fs, center wavelength of 400 nm, repetition rate of 1 kHz) were obtained by frequency doubling of pulses from a Ti:sapphire laser amplifier. Probe pulses (40 fs, 800 nm, 80 MHz) were taken from the seed oscillator of the amplifier.<sup>50</sup> Upon reflection off the sample, the probe polarization has acquired an additional rotation and ellipticity, part of which is proportional to the sample magnetization averaged over the probing volume (magneto-optic Kerr effect, MOKE).

The pump-induced polarization variation of the reflected probe pulse was measured using a balanced detection scheme. Rotation and ellipticity signals had the same dynamics, indicating negligible pump-induced variation of magneto-optic constants. We confirmed that the response was linear with respect to the used pump fluence of up to 1 mJ/cm<sup>2</sup>. To push the time resolution down to 130 fs, the pump-probe transient was deconvoluted with the pump-pulse profile.

**Spin-dynamics model.** Our goal is to model the spin dynamics of a single thin ferromagnetic metal layer F and an F|N stack where F is in contact with a thin normal-metal layer N. We assume that each layer X (F or N) can be treated as homogeneous and that the state of the electronic system in a given layer X is fully characterized by the occupation numbers  $n_k^{X\sigma}$  of a Bloch state  $(k, \sigma)$ . Here,  $\sigma = \uparrow, \downarrow$  refers to

the electron spin, and  $k$  summarizes the band index and wavevector. We define the magnetic moment  $\mathbf{m} = m\mathbf{u}_y$  of F such that  $(g^F/2)\mu_B m = MV^F$  where  $\mathbf{M} = M\mathbf{u}_y$  is the magnetization (Fig. 1a),  $g^F$  is the electron  $g$ -factor,  $\mu_B$  is the Bohr magneton, and  $V^F$  is the volume of F.

We adopt a simplified description in which the occupation of each Bloch state  $(k, \sigma)$  is fully given by its energy  $\epsilon_k^\sigma(t)$ , that is,

$$n_k^{X\sigma}(t) = n^{X\sigma}(\epsilon_k^{X\sigma}(t), t). \quad (11)$$

To model magnetic order, we make use of the Stoner model, in which the Bloch energy depends on the pump-induced change  $\Delta m$  in the magnetic moment according to

$$\epsilon_k^{X\sigma}(t) = \epsilon_{k0}^{X\sigma} + I^{X\sigma} \Delta m(t) + e\Phi^X(t). \quad (12)$$

Here,  $\epsilon_{k0}^{X\sigma}$  is the Bloch energy before arrival of the pump pulse, and  $I^{X\sigma} = I^{X\uparrow, \downarrow} = \pm I^X/2$  quantifies the strength of the effective electron-electron Coulomb interaction for  $X=F$  only. The electrostatic potential  $\Phi^X$  accounts for a possible charging of a given layer X due to transport, where  $-e$  is the electron charge.

Before arrival of the pump pulse, the  $n^{X\sigma}(\epsilon, t)$  are given by one and the same Fermi-Dirac function  $n_0(\epsilon)$  at temperature  $T_0$ . We now focus on the rate of change of the electron occupation numbers  $n^{F\sigma}$  in F. As detailed in the following, it is determined by four contributions,

$$\dot{n}^{F\sigma} = \dot{n}^{F\sigma}|_{sc} + \dot{n}^{F\sigma}|_{sf} + \dot{n}^{F\sigma}|_{tr} + \dot{n}^{F\sigma}|_I. \quad (13)$$

The first term on the right-hand side of Eq. (13) captures spin-conserving scattering events and the excitation by the pump pulse. It, thus, fulfills

$$0 = \int d\epsilon D^{F\sigma} \dot{n}^{F\sigma}|_{sc}, \quad (14)$$

where  $D^{X\sigma}(\epsilon, t) = \sum_k \delta(\epsilon - \epsilon_k^{X\sigma}(t))$  is the instantaneous density of Bloch states with spin  $\sigma$ .

Spin-flip events are captured by the second term of Eq. (13) and assumed to be quasi-elastic following Refs. 7 and 40. As indicated by Fig. 1c, the rate of change of the electron occupation  $n^{F\uparrow}$  due to elastic spin-flip scattering is proportional to  $n^{F\uparrow}$  and the number  $(1 - n^{F\downarrow})D^{F\downarrow}$  of available unoccupied spin-down states at the same energy  $\epsilon$  plus an analogous term for the reverse process,

$$\dot{n}^{F\uparrow}|_{sf} = -P_{sf}^F n^{F\uparrow} (1 - n^{F\downarrow}) D^{F\downarrow} + P_{sf}^F n^{F\downarrow} D^{F\downarrow} (1 - n^{F\uparrow}) = -(n^{F\uparrow} - n^{F\downarrow}) \frac{g_{sf}}{D^{F\uparrow}}. \quad (15)$$

Here,  $g_{sf}(\epsilon) = (P_{sf}^F D^{F\uparrow} D^{F\downarrow})(\epsilon)$ , and the factor  $P_{sf}(\epsilon)$  is proportional to the square of the matrix element for a spin-flip scattering event. The analogous equation for the rate of change of  $n^\downarrow(\epsilon)$  is obtained by simply swapping  $\uparrow$  and  $\downarrow$ .

The third term of Eq. (13) captures spin transfer across the F-N interface (see Fig. 1d). We assume the transmission events to be spin-conserving and elastic. Consequently, we can consider spin-up ( $\sigma = \uparrow$ ) and spin-down ( $\sigma = \downarrow$ ) electrons separately. By counting transmission events analogous to Eq. (15), we obtain

$$\dot{n}^{F\sigma}|_{tr} = -(n^{F\sigma} - n^{N\sigma}) \frac{g_{tr}^\sigma}{D^{F\sigma}}, \quad (16)$$

where  $g_{tr}^\sigma(\epsilon) = (T_{tr}^\sigma D^{F\sigma} D^{N\sigma})(\epsilon)$ , and  $T_{tr}^\sigma(\epsilon)$  is a spin-dependent interface transmittance.

The last term of Eq. (13) arises because  $n$  is evaluated at a fixed  $\epsilon$  while the Bloch energy changes according to Eq. (12). We obtain

$$\dot{n}^{F\sigma}|_I = n^{F\sigma'} I^{F\sigma} \dot{m} = I^{F\sigma} (\partial_\epsilon n^{F\sigma}) (\dot{m}|_{sf} + \dot{m}|_{tr}), \quad (17)$$

where  $n^{F\sigma'} = \partial n^{F\sigma} / \partial \epsilon$ . In the last step of Eq. (17), we split the rate of change of the magnetization into the contributions of spin flips and spin transport. As the electronic band structure depends on the magnetic moment  $m$  (see Eq. (12)),  $D^{F\sigma}(\epsilon)$ ,  $g_{sf}(\epsilon)$  and  $g_{tr}^\sigma(\epsilon)$  are also time-dependent. This time dependence is left implicit in our discussion.

**Spin transfer rates.** We are interested in the dynamics of the F magnetic moment

$$m = \int d\epsilon (D^{F\uparrow}n^{F\uparrow} - D^{F\downarrow}n^{F\downarrow}). \quad (18)$$

Using Eq. (15), its rate of change due to spin-flip events is given by

$$\dot{m}|_{sf} = -2 \int d\epsilon (n^{F\uparrow} - n^{F\downarrow}) g_{sf}^F. \quad (19)$$

Using Eq. (16), the spin-resolved electron current through the F-N interface can be calculated by

$$j^\sigma = \int d\epsilon (n^{F\sigma} - n^{N\sigma}) g_{tr}^\sigma. \quad (20)$$

We note that Eqs. (19) and (20) yield zero spin transfer before the pump pulse arrives because in this case, all distribution functions  $n^{F\sigma}$  and  $n^{N\sigma}$  equal the same Fermi-Dirac distribution  $n_0$  with chemical potential  $\mu_0$  and temperature  $T_0$ .

**Moment expansion.** As the relevant observables  $\dot{m}|_{sf}$  and  $j^\sigma$  involve differences of distribution functions only, we focus our discussion on the difference

$$\Delta n^{X\sigma} = n^{X\sigma} - n_0 \quad (21)$$

of the distribution function  $n^{X\sigma}(\epsilon, t)$  and the equilibrium distribution  $n_0$ . We assume that  $\Delta n^{X\sigma}$  is significantly nonzero only in a relatively narrow energy window around the chemical potential  $\mu_0$  of the unperturbed system and that the energy-dependent weight factors  $D^{F\sigma}(\epsilon)$ ,  $g_{sf}(\epsilon)$  and  $g_{tr}^\sigma(\epsilon)$  can be well approximated by

$$W(\epsilon) \approx W(\mu_0) + W'(\mu_0)(\epsilon - \mu_0), \quad (22)$$

where  $W$  stands for  $D^{F\sigma}$ ,  $g_{sf}$  or  $g_{tr}^\sigma$ . Integrals involving these functions, such as Eqs. (19) and (20), then turn into

$$\int d\epsilon W(\epsilon) \Delta n^{X\sigma}(\epsilon) = W(\mu_0) \Delta P^{X\sigma} + W'(\mu_0) \Delta A^{X\sigma}, \quad (23)$$

which is just a linear combination of the zeroth and first moment of  $\Delta n^\sigma$ , that is,

$$\Delta P^{X\sigma} = \int d\epsilon \Delta n^{X\sigma} \quad \text{and} \quad \Delta A^{X\sigma} = \int d\epsilon (\epsilon - \mu_0) \Delta n^{X\sigma}. \quad (24)$$

In the case that  $n^{X\sigma} = n_0 + \Delta n^{X\sigma}$  is a Fermi-Dirac distribution with chemical potential  $\mu^{X\sigma}$  and temperature  $T^{X\sigma}$ ,  $\Delta P^{X\sigma}$  and  $\Delta A^{X\sigma}$  reduce to

$$\Delta P^{X\sigma} = \mu^{X\sigma} - \mu_0 \quad \text{and} \quad \Delta A^{X\sigma} = \frac{\pi^2 k_B^2}{6} [(T^{X\sigma})^2 - T_0^2] + \frac{1}{2} (\mu^{X\sigma} - \mu_0)^2. \quad (25)$$

Because  $(\mu^{X\sigma} - \mu_0)^2$  is typically small, one can interpret  $\Delta P^\sigma$  and  $\Delta A^\sigma$ , respectively, as changes in a generalized chemical potential and a squared generalized temperature. We emphasize, however, that the definition of the moments  $\Delta P^{X\sigma}$  and  $\Delta A^{X\sigma}$  (Eq. (24)) also applies to nonthermal electron distributions  $n_0 + \Delta n^{X\sigma}$ .

In Ref. 39, the difference  $\Delta\mu_s = \Delta\mu^{F\uparrow} - \Delta\mu^{F\downarrow}$  is termed spin voltage. We accordingly term

$$\Delta P_s = \Delta P^{F\uparrow} - \Delta P^{F\downarrow} \quad (26)$$

generalized spin voltage. In the main text,  $\Delta P_s$  is written as  $\Delta \tilde{\mu}_s$ , and further below (Eq. (36)), we will express  $\Delta A^{X\sigma}$  by the generalized excess temperature  $\Delta \tilde{T}^{X\sigma}$  of the  $X\sigma$  electrons.

As the pump-induced variation of the electron distribution functions  $n^{X\sigma}$  and, thus, the transient state of the electronic system are fully characterized by the moments  $\Delta P^{X\sigma}$  and  $\Delta A^{X\sigma}$ , it is sufficient to determine the dynamics of  $\Delta P^{X\sigma}$  and  $\Delta A^{X\sigma}$ . This conclusion is consistent with a recent phenomenological treatment of ultrafast spin dynamics.<sup>40</sup> In the following, we will connect the phenomenological coupling coefficients of Ref. 40 with the parameters of our simplified microscopic description.

**Relevant observables.** We apply Eq. (23) to the rate of change of the magnetic moment (Eq. (19)). We find

$$\dot{m}|_{sf} = -2g_{sf}(\mu_0)\Delta P_s - 2g'_{sf}(\mu_0)(\Delta A^{F\uparrow} - \Delta A^{F\downarrow}), \quad (27)$$

where the first term on the right-hand side describes magnetization relaxation driven by the generalized spin voltage (Eq. (26)). The term proportional to  $\Delta A^{F\uparrow} - \Delta A^{F\downarrow}$  is a term analogous to the Seebeck effect, which contributes as long as the generalized temperatures of spin-up and spin-down electrons are different.

The magnetic moment of F is also modified by spin transport through the F-N interface,  $-\dot{m}|_{tr} = j_s = j^\uparrow - j^\downarrow$ . We assume vanishing charge transport,  $j^\uparrow + j^\downarrow = 0$ , and the same chemical potential for spin-up and spin-down electrons in the N layer,  $\Delta P^{N\uparrow} = \Delta P^{N\downarrow} = \Delta P^N$ . These assumptions allow us to eliminate  $\phi^N - \phi^F$  (see Supplementary Note 2). Along with Eqs. (20), (23) and (24), we find

$$-\dot{m}|_{tr} = j_s = g_{tr}(\mu_0)\Delta P_s + s_{tr}^\uparrow(\mu_0)(\Delta A^{F\uparrow} - \Delta A^{N\uparrow}) - s_{tr}^\downarrow(\mu_0)(\Delta A^{F\downarrow} - \Delta A^{N\downarrow}), \quad (28)$$

where  $2g_{tr}^{-1} = (g_{tr}^\uparrow)^{-1} + (g_{tr}^\downarrow)^{-1}$  and  $s_{tr}^\sigma = g_{tr}g_{tr}^{\sigma'}/g_{tr}^\sigma$ . The two final terms in Eq. (28) are again of Seebeck type and vanish once the temperatures of the F and N layer have equilibrated. In this regime, the driving force of both  $\dot{m}^F|_{sf}$  and  $\dot{m}^F|_{tr}$  is given solely by the spin voltage  $\Delta P_s$  of F.

The total energy of the F electrons is in the Stoner model given by  $E^F = \sum_\sigma \int d\epsilon (\epsilon - \mu_0)D^{F\sigma}n^{F\sigma} + I^F m^2/4$ . By using  $\dot{D}^{F\sigma}(\epsilon) = D^{F\sigma'}(\epsilon)I^{F\sigma}\dot{m}$  and Eq. (18), we find that the rate of change obeys

$$\dot{E}^F = \sum_\sigma \int d\epsilon (\epsilon - \mu_0)D^{F\sigma}(\dot{n}^{F\sigma} - \dot{n}^{F\sigma}|_I), \quad (29)$$

where the term  $\dot{n}^{F\sigma}|_I$  (Eq. (17)) takes the time-dependence of the Bloch energies into account.

**Time evolution of  $\Delta P_s$ .** To determine the dynamics of the system and, thus, the magnetization, it is sufficient to determine the dynamics of the moments, that is, the generalized spin voltage  $\Delta P_s$  and squared temperatures  $\Delta A^{X\sigma}$ . According to Eqs. (13) and (17), we need to consider contributions of spin flips, spin transport and spin-conserving processes,

$$\Delta \dot{P}_s = \Delta \dot{P}_s|_{sf} + \Delta \dot{P}_s|_{tr} + \Delta \dot{P}_s|_{sc}. \quad (30)$$

By taking the time derivative of Eq. (24), considering Eqs. (15) and (17), performing the moment expansion of Eq. (23), and using Eq. (27), we obtain (see Supplementary Note 2)

$$\Delta \dot{P}_s|_{sf} = -\frac{2}{\chi^F(\mu_0)} [g_{sf}(\mu_0)\Delta P_s + s_{sf}(\mu_0)(\Delta A^{F\uparrow} - \Delta A^{F\downarrow})], \quad (31)$$

where  $1/\chi^F = (1/D^{F\uparrow} + 1/D^{F\downarrow})/2 - I^F$  is the inverse of the Pauli susceptibility  $\chi^F = \partial m / \partial \mu_s$  of F, and  $s_{sf} = g'_{sf} - (1/2)\chi^F g_{sf} [D^{F\uparrow'}/(D^{F\uparrow})^2 + D^{F\downarrow'}/(D^{F\downarrow})^2]$  is the coefficient describing the Seebeck-type response of the spin voltage to a temperature difference between majority and minority electrons.

To determine the contribution of spin transport, we take the time derivative of Eq. (24), consider Eqs. (16) and (17), perform the moment expansion of Eq. (23) and use Eq. (28). Making the same assumptions as in the derivation of Eq. (28), we obtain (see Supplementary Note 2)

$$\Delta\dot{P}_s|_{\text{tr}} = -\frac{1}{\chi^F(\mu_0)} [g_{\text{tr}}(\mu_0)\Delta P_s + \tilde{s}_{\text{tr}}^{\uparrow}(\mu_0)(\Delta A^{F\uparrow} - \Delta A^{N\uparrow}) - \tilde{s}_{\text{tr}}^{\downarrow}(\mu_0)(\Delta A^{F\downarrow} - \Delta A^{N\downarrow})], \quad (32)$$

where  $\tilde{s}_{\text{tr}}^{\sigma} = s_{\text{tr}}^{\sigma} - g_{\text{tr}}^{\sigma'}\chi^F/D^{F\sigma}$ .

Excitation by the pump pulse and subsequent spin-conserving electron-electron and electron-lattice interactions also affect the occupation numbers  $n^{X\sigma}$ . By applying the moment expansion of Eq. (23) to Eq. (14), we find that spin-conserving scattering processes couple the spin voltage and the generalized temperature through

$$\Delta\dot{P}_s|_{\text{sc}} = -\frac{D^{F\uparrow'}}{D^{F\uparrow}}(\mu_0)\Delta\dot{A}^{F\uparrow}|_{\text{sc}} + \frac{D^{F\downarrow'}}{D^{F\downarrow}}(\mu_0)\Delta\dot{A}^{F\downarrow}|_{\text{sc}}. \quad (33)$$

Equation (30) along with Eqs. (31), (32) and (33) determine the dynamics of the spin voltage, provided the dynamics of the generalized squared temperature  $\Delta A^{X\sigma}$  are given. In these equations, the prefactors of  $\Delta A^{X\sigma}$  and  $\Delta P_s$  depend on the instantaneous state of the system and, thus, on the time-dependent occupation numbers  $n^{X\sigma} = n_0 + \Delta n^{X\sigma}$ .

**Linear excitation limit.** From now on, we focus on the limit of weak optical excitation of the F and F|N samples. In fact, in our experiments, all terahertz emission signals were found to scale linearly with the incident pump-pulse energy up to the maximum available incident fluence of 0.2 mJ/cm<sup>2</sup>. Therefore,  $\dot{m}$  and  $j_s$  and, through Eqs. (27) and (28),  $\Delta P_s$  and  $\Delta A^{X\sigma}$ , and, by Eq. (24), the changes in the occupation numbers  $\Delta n^{X\sigma}$  are also directly proportional to the deposited pump power. It follows that the prefactors in Eqs. (31), (32) and (33) are independent of the pump-induced changes  $\Delta n^{X\sigma}$  in the occupation numbers and can, thus, be evaluated for the unperturbed system. This simplification has important consequences.

First, we can solve Eq. (30) along with Eqs. (31), (32) and (33) for the spin voltage  $\Delta P_s$ . We find that  $\Delta P_s$  is a convolution

$$\Delta P_s(t) = -(H_{\text{es}} * \Delta F)(t) = -\int d\tau H_{\text{es}}(t - \tau)\Delta F(\tau) \quad (34)$$

of a driving force  $\Delta F$  with a response function  $H_{\text{es}}(t) = \Theta(t)e^{-\Gamma_{\text{es}}t}$ , where  $\Theta(t)$  is the Heaviside step function. The exponential decay rate equals  $\Gamma_{\text{es}} = g_{\text{sf}}/\chi^F$  for the F sample and  $\Gamma_{\text{es}} = (g_{\text{sf}} + g_{\text{tr}})/\chi^F$  for the F|N stack. The expression for the driving force  $\Delta F$  is

$$\Delta F = \frac{D^{F\uparrow'}}{D^{F\uparrow}}\Delta\dot{A}^{F\uparrow}|_{\text{sc}} - \frac{D^{F\downarrow'}}{D^{F\downarrow}}\Delta\dot{A}^{F\downarrow}|_{\text{sc}} + \frac{S_{\text{sf}}}{\chi^F}(\Delta A^{F\uparrow} - \Delta A^{F\downarrow}) + \frac{\tilde{s}_{\text{tr}}^{\uparrow}}{\chi^F}(\Delta A^{F\uparrow} - \Delta A^{N\uparrow}) - \frac{\tilde{s}_{\text{tr}}^{\downarrow}}{\chi^F}(\Delta A^{F\downarrow} - \Delta A^{N\downarrow}), \quad (35)$$

where all coefficients should be evaluated at  $\epsilon = \mu_0$  and for the unperturbed system. The first two terms of  $\Delta F$  cause a change in the spin voltage and scale with the time derivative of the pump-induced excess energy of spin-up and spin-down electrons. The remaining terms are Seebeck-type terms that disappear when the generalized temperatures of all electron subsystems  $X\sigma$  have the same value. The last two terms in Eq. (35) are omitted for the case of an F sample.

Second, the pump-induced change in the squared generalized temperature (Eq. (25)) of electron system  $X\sigma$  simplifies to

$$\Delta A^{X\sigma} = \frac{\pi^2 k_{\text{B}}^2}{3} T_0 \Delta \tilde{T}^{X\sigma}, \quad (36)$$

where  $T_0 + \Delta \tilde{T}^{X\sigma}$  can be interpreted as generalized temperature of the  $X\sigma$  electrons. The expression for the generalized chemical potential  $\mu_0 + \Delta P^{X\sigma} = \mu_0 + \Delta \tilde{\mu}^{X\sigma}$  remains unchanged.

Third, the rate of change of the energy of the X-layer electrons (see Eq. (29)) simplifies to

$$\dot{E}^F = \sum_{\sigma} \int d\epsilon (\epsilon - \mu_0) D_0^{F\sigma} \dot{n}^{F\sigma} = \sum_{\sigma} C_e^{F\sigma} \partial_t \Delta \tilde{T}^{F\sigma} \quad (37)$$

where  $C_e^{X\sigma} = (\pi^2 k_B^2/3) T_0 D_0^{X\sigma}(\mu_0)$  is the heat capacity of the  $X\sigma$  electrons. Here, we neglected terms of order  $(\epsilon - \mu_0)^2$  and higher, and in the last step of Eq. (29), the moment expansion of Eq. (24) was used. Therefore, the excess energy of the F-layer electrons is

$$\Delta E^F = \sum_{\sigma} C_e^{X\sigma} \Delta \tilde{T}^{X\sigma}, \quad (38)$$

which underscores the interpretation of  $T_0 + \Delta \tilde{T}^{X\sigma}$  as generalized temperature.

**Dynamics of excess energy.** Owing to Eqs. (27), (28), (34) and (35), the dynamics of UDM and TST are fully determined by a linear combination of the  $\Delta A^{X\sigma}$  and, because of Eq. (36), the generalized excess temperatures  $\Delta \tilde{T}^{X\sigma}$  of all electron subsystems  $X\sigma$ .

To develop a simple model for the time dependence of the generalized temperature, we briefly review the processes following photoexcitation of metal thin films.<sup>42</sup> At time  $t = 0$ , the  $\delta$ -like pump pulse excites the sample, thereby causing a step-like increase of the electronic excess energy and, thus, of all  $\Delta \tilde{T}^{X\sigma}$ .

Due to electron-electron interactions, all electronic subsystems  $X\sigma$  quickly reach thermal equilibrium with each other, resulting in approximately equal generalized electronic temperatures,  $\Delta \tilde{T}^{X\sigma} = \Delta \tilde{T}_e$ . In this limit, the Seebeck-type contributions to the magnetization dynamics (Eqs. (27) and (28)) and to the driving force  $\Delta F$  (Eq. (35)) are absent. Because we do not observe any signature Seebeck-type terms in our experiment, we assume one uniform electron temperature ( $\Delta \tilde{T}^{X\sigma} = \Delta \tilde{T}_e$ ) at all times. As a consequence, Eqs. (34), (35) and (36) result in Eq. (6) of the main text. As mentioned above, carrier multiplication is not relevant for modifying the excess energy and, thus,  $\Delta \tilde{T}^{X\sigma}$ .

Electron-phonon interaction, on the other hand, causes heat transfer from the electrons to the crystal lattice with time constant  $\Gamma_{ep}^{-1}$ . On a much longer time scale, which is not considered here, heat is transferred into the sample environment. Consequently, we model the time dependence of the generalized temperature by the ansatz

$$\Delta \tilde{T}_e(t) = \Theta(t) [\Delta \tilde{T}_{e0} + (\Delta \tilde{T}_{e0} - \Delta \tilde{T}_{\infty}) e^{-\Gamma_{ep} t}]. \quad (39)$$

Here,  $\Delta \tilde{T}_{e0}$  is the increase of the uniform generalized temperature after absorption of the  $\delta(t)$ -like pump pulse and the fast equilibration between all electron subsystems  $X\sigma$ . The term  $\Delta \tilde{T}_{\infty} = R \Delta \tilde{T}_{e0}$  is the generalized excess temperature at which the combined electron and lattice system equilibrate, with  $R$  being the ratio of electronic and total heat capacity. The driving force  $\Delta F$  for the spin voltage then assumes the simple form

$$\Delta F = \gamma \partial_t \Delta \tilde{T}_e = \gamma \Delta \tilde{T}_{e0} [\delta(t) - (1 - R) \Gamma_{ep} \Theta(t) e^{-\Gamma_{ep} t}], \quad (40)$$

where we abbreviated  $\gamma = (\pi^2 k_B^2 T_0/3) (D^{F\uparrow'}/D^{F\uparrow} - D^{F\downarrow'}/D^{F\downarrow})_0(\mu_0)$ . Using Eq. (34), one immediately finds that

$$\Delta P_s(t) = -\gamma \Delta \tilde{T}_{e0} \Theta(t) \left[ \frac{\Gamma_{es} - R \Gamma_{ep}}{\Gamma_{es} - \Gamma_{ep}} e^{-\Gamma_{es} t} - \frac{(1 - R) \Gamma_{ep}}{\Gamma_{es} - \Gamma_{ep}} e^{-\Gamma_{ep} t} \right]. \quad (41)$$

Without the Seebeck-type contributions,  $\dot{m}|_{sf}$  (Eq. (27)) and  $\dot{m}|_{tr} = -j_s$  (Eq. (28)) are both directly proportional to  $\Delta P_s(t)$ , and Eq. (41) turns into Eq. (7) of the main text. To account for the time resolution of our experiment, we convolute Eq. (41) with a Gaussian of 40 fs full width at half maximum.

To fit our data with Eq. (41), we obtain  $\Gamma_{\text{ep}}$  and  $R$  from previous works and Eqs. (42) and (43). Prior to fitting, all measured curves are shifted to the same time zero. The only fit parameters are  $\Gamma_{\text{es}}$  and an overall scaling factor. As seen in Fig. 4, we obtain excellent agreement with our measurements. All parameters and references are summarized in Supplementary Table S1.

**Extended two-temperature model.** To determine  $\Gamma_{\text{ep}}$  and  $R$  for an F sample, we make use of the standard two-temperature model.<sup>42</sup> To model the decay of the electronic excess heat in the F|N stack, we assume that equilibration between electron baths of different spins and in different layers is much faster than electron-phonon equilibration. Therefore, all electron baths  $X\sigma$  can be described by one common generalized excess temperature  $\Delta\tilde{T}_e = \Delta\tilde{T}^{X\sigma}$ , consistent with the notion of negligible Seebeck terms in Eq. (35). The phonon bath of each layer couples to the electrons of the same layer. The energy-flow diagrams, differential equations and their solution are detailed in Supplementary Note 2.

We find that for the time scales relevant to our experiment, the dynamics of the generalized electron excess temperature is given by Eq. (39) with

$$\Gamma_{\text{ep}} = \frac{G_{\text{ep}}^F + G_{\text{ep}}^N}{C_e^F + C_e^N} \quad (42)$$

and

$$R = \frac{C_e^F + C_e^N}{C_e^F + C_e^N + C_p^F + C_p^N}. \quad (43)$$

Here,  $C_e^X$  and  $C_p^X$  are the heat capacities of electrons and phonons of X, respectively, and  $G_{\text{ep}}^X$  quantifies electron-phonon coupling in X. For an F sample, the parameters  $\Gamma_{\text{ep}}$  and  $R$  are obtained by setting  $C_e^N = 0$  and  $G_{\text{ep}}^N = 0$  in Eqs. (42) and (43).

Note that the  $C_e^X$ ,  $C_p^X$  and  $G_{\text{ep}}^X$  are extensive quantities because they refer to the F and N volumes that are effectively coupled to each other in terms of ultrafast energy exchange. For our stack geometry, we assume equal coupling lengths into the depth of F and N. Therefore, we can replace the extrinsic quantities  $C_e^X$ ,  $C_p^X$  and  $G_{\text{ep}}^X$  by their specific (volume-normalized) counterparts, which can be obtained from literature (see Supplementary Table S1).

## Acknowledgments

We thank Dr. Yuta Sasaki for contributions in an early stage of this work. We acknowledge funding by the German Science Foundation through the collaborative research center SFB TRR 227 “Ultrafast spin dynamics” (projects A05, B01, B02 and B03) and the priority program SPP 1666 “Topological Insulators” and funding by European Union through the ERC H2020 CoG project TERAMAG/Grant No. 681917. R.R. acknowledges support by the IMPRS for Elementary Processes in Physical Chemistry.

## Note added

When this manuscript was completed for submission, we became aware of a work part of which addresses a related topic: Lichtenberg, T., Beens, M., Jansen, M.H., Duine, R.A., Koopmans, B. Probing optical spin-currents using THz spin-waves in noncollinear magnetic bilayers, arXiv:2103.06029 [cond-mat.mes-hall].

## References

<sup>1</sup> Vedmedenko, E.Y. *et al.*, The 2020 Magnetism Roadmap, *J. Phys. D: Appl. Phys.* **53**, 453001 (2020)

<sup>2</sup> Kirilyuk, A., Kimel, A. V & Rasing, T. Ultrafast optical manipulation of magnetic order. *Rev. Mod. Phys.* **82**, 2731–2784 (2010).

<sup>3</sup> Kirilyuk, A., Kimel, A. V. & Rasing, T. Laser-induced magnetization dynamics and reversal in ferrimagnetic alloys. *Rep. Prog. Phys.* **76**, 026501 (2013).

<sup>4</sup> Walowski, J. & Münzenberg, M. Perspective: Ultrafast magnetism and THz spintronics. *Journal of Applied Physics* **120**, 140901 (2016)

<sup>5</sup> Malinowski, G., Bergeard, N., Hehn, M. & Mangin, S. Hot-electron transport and ultrafast magnetization dynamics in magnetic multilayers and nanostructures following femtosecond laser pulse excitation. *The European Physical Journal B* **91**, 1-20 (2018).

<sup>6</sup> Eschenlohr, A. Spin dynamics at interfaces on femtosecond timescales. *J. Phys.: Condens. Matter* **33**, 013001 (2020).

<sup>7</sup> Beaurepaire, E., Merle, J.-C., Daunois, A. & Bigot, J.-Y. Ultrafast Spin Dynamics in Ferromagnetic Nickel. *Phys. Rev. Lett.* **76**, 4250–4253 (1996).

<sup>8</sup> Hohlfeld, J., Matthias, E., Knorren, R. & Bennemann, K. H. Nonequilibrium Magnetization Dynamics of Nickel. *Phys. Rev. Lett.* **78**, 4861–4864 (1997).

<sup>9</sup> Koopmans, B. *et al.* Explaining the paradoxical diversity of ultrafast laser-induced demagnetization. *Nat. Mater.* **9**, 259–265 (2010).

<sup>10</sup> Carva, K., Battiato, M. & Oppeneer, P. M. Ab Initio Investigation of the Elliott-Yafet Electron-Phonon Mechanism in Laser-Induced Ultrafast Demagnetization. *Phys. Rev. Lett.* **107**, 207201 (2011).

<sup>11</sup> Mueller, B. Y. *et al.* Feedback Effect during Ultrafast Demagnetization Dynamics in Ferromagnets. *Phys. Rev. Lett.* **111**, 167204 (2013).

<sup>12</sup> Töws, W. & Pastor, G. M. Many-Body Theory of Ultrafast Demagnetization and Angular Momentum Transfer in Ferromagnetic Transition Metals. *Phys. Rev. Lett.* **115**, 217204 (2015).

<sup>13</sup> Manchon, A., Li, Q., Xu, L. & Zhang, S. Theory of laser-induced demagnetization at high temperatures. *Phys. Rev. B* **85**, 64408 (2012).

<sup>14</sup> Krieger, K., Dewhurst, J. K., Elliott, P., Sharma, S. & Gross, E. K. U. Laser-Induced Demagnetization at Ultrashort Time Scales: Predictions of TDDFT. *J. Chem. Theory Comput.* **11**, 4870–4874 (2015).

<sup>15</sup> Malinowski, G. *et al.* Control of speed and efficiency of ultrafast demagnetization by direct transfer of spin angular momentum. *Nat. Phys.* **4**, 855–858 (2008).

<sup>16</sup> Rudolf, D. *et al.* Ultrafast magnetization enhancement in metallic multilayers driven by superdiffusive spin current. *Nat. Commun.* **3**, 1037 (2012).

<sup>17</sup> Eschenlohr, A. *et al.* Ultrafast spin transport as key to femtosecond demagnetization. *Nat. Mat.* **12**, 332–336 (2013).

<sup>18</sup> Kampfrath, T. *et al.* Terahertz spin current pulses controlled by magnetic heterostructures. *Nat. Nanotechnol.* **8**, 256–260 (2013).

<sup>19</sup> Choi, G.-M. *et al.* Spin current generated by thermally driven ultrafast demagnetization. *Nat. Commun.* **5**:4334 doi: 10.1038/ncomms5334 (2014).

<sup>20</sup> Fognini, A., Michlmayr, T. U., Vaterlaus, A. & Acremann, Y. Laser-induced ultrafast spin current pulses: a thermodynamic approach. *J. Phys.: Condensed Matter* **29**, 214002 (2017).

<sup>21</sup> Rzadolski, I. *et al.* Nanoscale interface confinement of ultrafast spin transfer torque driving non-uniform spin dynamics. *Nat. Commun.* **8**, 15007 (2017).

<sup>22</sup> Lalieu, M. L. M., Lavrijsen, R., Duine, R. A. & Koopmans, B. Investigating optically excited terahertz standing spin waves using noncollinear magnetic bilayers. *Phys. Rev. B* **99**, 184439 (2019).

<sup>23</sup> Seifert, T. *et al.* Efficient metallic spintronic emitters of ultrabroadband terahertz radiation. *Nat. Photonics* **10**, 483-488 (2016).

<sup>24</sup> Yang, D. *et al.* Powerful and Tunable THz Emitters Based on the Fe/Pt Magnetic Heterostructure. *Adv. Opt. Mater.* **4**, 1944–1949 (2016).

<sup>25</sup> Wu, Y. *et al.* High-Performance THz Emitters Based on Ferromagnetic/Nonmagnetic Heterostructures. *Adv. Mater.* **29**, 1603031 (2017).

<sup>26</sup> Torosyan, G., Keller, S., Scheuer, L., Beigang, R. & Papaioannou, E. T. Optimized Spintronic Terahertz Emitters Based on Epitaxial Grown Fe/Pt Layer Structures. *Sci. Rep.* **8**, 1311 (2018).

<sup>27</sup> Battiatto, M., Carva, K. & Oppeneer, P. M. Superdiffusive Spin Transport as a Mechanism of Ultrafast Demagnetization. *Phys. Rev. Lett.* **105**, 27203 (2010).

<sup>28</sup> Nenno, D. M., Kaltenborn, S. & Schneider, H. C. Boltzmann transport calculation of collinear spin transport on short timescales. *Phys. Rev. B* **94**, 115102 (2016).

<sup>29</sup> Hurst, J., Hervieux, P.-A. & Manfredi, G. Spin current generation by ultrafast laser pulses in ferromagnetic nickel films. *Phys. Rev. B* **97**, 014424 (2018).

<sup>30</sup> Beaurepaire, E. *et al.* Coherent terahertz emission from ferromagnetic films excited by femtosecond laser pulses. *Applied Phys. Lett.* **84**, 3465–3467 (2004).

<sup>31</sup> Zhang, W. *et al.* Ultrafast terahertz magnetometry. *Nat. Commun.* **11**, 4247 (2020).

<sup>32</sup> Seifert, T. S. *et al.* Frequency-Independent Terahertz Anomalous Hall Effect in DyCo<sub>5</sub>, Co<sub>32</sub>Fe<sub>68</sub>, and Gd<sub>27</sub>Fe<sub>73</sub> Thin Films from DC to 40 THz. *Adv. Mater.* 2007398 (2021).

<sup>33</sup> Leitenstorfer, A. *et al.* Detectors and sources for ultrabroadband electro-optic sampling: experiment and theory. *Appl. Phys. Lett.* **74**, 1516 (1999).

<sup>34</sup> Braun, L. *et al.* Ultrafast photocurrents at the surface of the three-dimensional topological insulator Bi<sub>2</sub>Se<sub>3</sub>. *Nat. Commun.* **7**, 13259 (2016).

<sup>35</sup> Seifert, T. S. *et al.* Femtosecond formation dynamics of the spin Seebeck effect revealed by terahertz spectroscopy. *Nat. Commun.* **9**, 2899 (2018).

<sup>36</sup> Ramakrishnan, G., Chakkittakandy, R. & Planken, P. C. M. Terahertz generation from graphite. *Optics Express* **17**, 16092 (2009).

<sup>37</sup> Zhang, Q. *et al.* Terahertz Emission from Anomalous Hall Effect in a Single-Layer Ferromagnet. *Phys. Rev. Applied* **12**, 054027 (2019).

<sup>38</sup> Meserole, C. A. *et al.* Growth of thin Fe(001) films for terahertz emission experiments. *Appl. Surf. Sci.* **253**, 6992–7003 (2007).

<sup>39</sup> Bühlmann, K., Saerens, G., Vaterlaus, A. & Acremann, Y. Detection of femtosecond spin voltage pulses in a thin iron film. *Struct. Dyn.* **7**, 65101 (2020).

<sup>40</sup> Mueller, B. Y. & Rethfeld, B. Thermodynamic  $\mu$ T model of ultrafast magnetization dynamics. *Phys. Rev. B* **90**, 144420 (2014).

<sup>41</sup> Bauer, G. E. W., Saitoh, E. & van Wees, B. J. Spin caloritronics. *Nat. Mater.* **11**, 391–399 (2012).

<sup>42</sup> Hohlfeld, J. *et al.* Electron and lattice dynamics following optical excitation of metals. *Chem. Phys.* **251**, 237–258 (2000).

<sup>43</sup> Mueller, B. Y. & Rethfeld, B. Relaxation dynamics in laser-excited metals under nonequilibrium conditions. *Phys. Rev. B* **87**, 35139 (2013).

<sup>44</sup> He, W., Zhu, T., Zhang, X.-Q., Yang, H.-T. & Cheng, Z.-H. Ultrafast demagnetization enhancement in CoFeB/MgO/CoFeB magnetic tunneling junction driven by spin tunneling current. *Sci. Rep.* **3**, 2883 (2013).

<sup>45</sup> Radu, I. *et al.* Ultrafast and Distinct Spin Dynamics in Magnetic Alloys. *Spin* **05**, 1550004 (2015).

<sup>46</sup> Willems, F. *et al.* Optical inter-site spin transfer probed by energy and spin-resolved transient absorption spectroscopy. *Nat. Commun.* **11**, 871 (2020).

<sup>47</sup> Turgut, E. *et al.* Controlling the competition between optically induced ultrafast spin-flip scattering and spin transport in magnetic multilayers. *Phys. Rev. Lett.* **110**, 197201 (2013).

<sup>48</sup> Kirihaara, A. *et al.* Spin-current-driven thermoelectric coating. *Nat. Mater.* **11**, 686–689 (2012).

<sup>49</sup> Gueckstock, O. *et al.* Terahertz Spin-to-Charge Conversion by Interfacial Skew Scattering in Metallic Bilayers. *Adv. Mat.* **33**, 2006281 (2021).

<sup>50</sup> Maehrlein, S.F. *et al.* Dissecting spin-phonon equilibration in ferrimagnetic insulators by ultrafast lattice excitation. *Sci. Adv.* **4**, eaar5164 (2018).